Stable water isotopes in the MITgcm (checkpoint 64w)

Rike Völpel [1], André Paul [1], Annegret Krandick[1], Stefan Mulitza [1] and Michael Schulz[1]

[1]MARUM - Center for Marine Environmental Sciences and Faculty of Geosciences, University of Bremen, Bremen, Germany

5 *Correspondence to*: Rike Völpel (rvoelpel@marum.de)

Abstract.

We present the first results of the implementation of stable water isotopes in the ocean general circulation model MITgcm. The model is forced with the isotopic content of precipitation and water vapor from an atmospheric general circulation model (NCAR IsoCAM), while the fractionation during evaporation is treated explicitly in the MITgcm. Results of the
10 equilibrium simulation under pre-industrial conditions are compared to observational data and paleoclimate records (the oxygen isotopic composition of planktic foraminiferal calcite). The broad patterns and magnitude of the stable water isotopes in annual mean seawater are well captured in the model, both at the sea surface as well as in the deep ocean. However, the surface water in the Arctic Ocean is not depleted enough, due to the absence of highly depleted precipitation and snow fall and slightly enriched river runoff. This shortcoming is also recognizable in the isotopic composition of the seawater-salinity
15 relationship in mid-latitudes. Deep ocean characteristics of the vertical water mass distribution in the Atlantic Ocean closely resemble observational data. Apart from the systematic offset of the modeled oxygen isotopic composition of planktic foraminiferal calcite towards lower values, the comparison with proxy data shows a good agreement. We summarize that the offset is mainly caused by gametogenic calcification and a matter of choice of the applied paleotemperature equation. Overall, the newly developed stable water isotope package opens wide prospects for long-term simulations in a paleoclimatic
20 context.

1 Introduction

Stable water isotopes ($H_2^{16}O$, $H_2^{18}O$ and $HD^{16}O$ = HDO) are widely used tracers of the hydrological cycle (Craig and Gordon, 1965; Gat and Gonfiantini, 1981) and can be used to determine the origin and mixing pattern of different water masses (e.g. Jacobs et al., 1985; Khatwala et al., 1999; Meredith et al., 1999). Due to differences in their physical and
25 chemical properties, stable water isotopes undergo fractionation processes at any phase transition within the hydrological cycle (Craig and Gordon, 1965). This leads to distinctive isotopic signatures for different freshwater fluxes, which are commonly expressed as δi (i = ^{18}O or D) with reference to the Vienna Standard Mean Ocean Water (VSMOW) standard and given as:

$$\delta i = \left(\frac{R}{R_{VSMOW}} - 1 \right) \cdot 1000 \text{ ‰} , \tag{1}$$

where R is the ratio of the abundance of the heavier water isotope $H_2^{18}O$ (HDO) to the abundance of the lighter isotope $H_2^{16}O$ and $R_{VSMOW} = 2005.2 \cdot 10^{-6}$ for $\delta^{18}O$ (Baertschi, 1976) and $155.95 \cdot 10^{-6}$ for δD (de Wit et al., 1980).

Stable water isotopes have been used as an important proxy in a wide range of climate archives e.g. to infer past temperatures from ice cores (Johnsen et al., 2001) or the amount of monsoonal rainfall from speleothems (Fleitmann et al.,
5 2003). As an indirect record, stable water isotopes are preserved in carbonates ($CaCO_3$) from marine species such as planktonic and benthic foraminifers. Due to the temperature-dependent fractionation effect that occurs during the formation of $CaCO_3$, the oxygen isotopic composition of foraminiferal $CaCO_3$ ($\delta^{18}O_c$) is a function of both the ambient temperature and the isotopic composition of the seawater ($\delta^{18}O_w$) in which the calcification takes place (Emiliani, 1955). Hence, $\delta^{18}O_c$ records form sediment cores provide information on water mass changes.

10 During the last few decades, stable water isotopes have been incorporated more extensively in general circulation models (GCMs). First realizations were made in atmospheric GCMs (AGCMs – Joussaume et al., 1984; Jouzel et al., 1987) and more than a decade later in oceanic GCMs (OGCMs – Schmidt, 1998; Paul et al., 1999; Wadley et al., 2002, Xu et al., 2012), which mainly focused on the linear relation between $\delta^{18}O_w$ and salinity, since they are affected by similar physical processes. This topic is of significant interest in paleoceanography, because it is likely that changes in advection and freshwater budgets
15 as well as the source of precipitation have altered the relationship (Rohling and Bigg, 1998). Using real freshwater flux boundary conditions in conjunction with the nonlinear free-surface (Huang, 1993) is essential to simulate this relationship properly. The Massachusetts Institute of Technology general circulation model (MITgcm) offers this very opportunity and further provides the adjoint method to perform data assimilation (Errico, 1997).

Here, we present first results of the implementation of stable water isotopes in the MITgcm, by performing an equilibrium
20 pre-industrial (PI) simulation and comparing it to available observations and reconstructions.

2 Methods

2.1 Ocean Model

The MITgcm ("checkpoint" 64w) was employed, solving the Boussinesq, hydrostatic Navier–Stokes equations and using a nonlinear free-surface configuration (Marshall et al., 1997; Adcroft et al., 2004b). A cubed-sphere grid was used which
25 provided a nearly uniform resolution and avoided pole singularities (Adcroft et al., 2004a). It consisted of 6 faces, each of which comprised 32 x 32 grid cells, resulting in a horizontal spatial resolution of approximately 2.8°. There were 15 vertical levels, ranging in thickness from 50 m at the surface to 690 m at the seafloor, giving a maximum model depth of 5200 m. Associated with the non-linear free-surface is the possible vanishing of the upper layer. To avoid this problem, the rescaled vertical coordinate z* was employed (Adcroft and Campin, 2004). Furthermore, the shaved cell formulation was used, which
30 reduced the representation error of the bathymetry (Adcroft et al., 1997). The model was coupled to a dynamic-thermodynamic sea ice model with a viscous-plastic rheology (Losch et al., 2010).

Isopycnal diffusion and eddy-induced mixing was parameterized with the GM/Redi scheme (Redi, 1982; Gent and McWilliams, 1990). Background vertical diffusivity for tracers was uniform at $3 \cdot 10^{-5}$ [$m^2 \ s^{-1}$], and for the equation of state the polynomial approximation of Jackett and McDougall (1995) was used. Advection of tracers was computed using third-order advection with direct space-time treatment (Hundsdorfer and Trompert, 1994).

5   Atmospheric forcing (air temperature, specific humidity, zonal and meridional wind velocity, wind speed, (snow-) precipitation, incoming shortwave and longwave radiation as well as river runoff – 12 months climatological means) was obtained from the PI ocean state estimate by Kurahashi-Nakamura et al., (submitted), which was based on the protocol of the Coordinated Ocean-ice Reference Experiments (COREs) project (Griffies et al., 2009). They optimized the forcing fields to reconstruct tracer distributions that were consistent with observations. Air-sea fluxes were internally computed in the model
10   following the bulk forcing approach by Large and Yeager (2004).

Our simulation was initialized with present-day salinity and temperature distributions (Levitus et al., 1994 and Levitus and Boyer 1994, respectively) and spun up from the state of rest. We used asynchronous time stepping to accelerate computation with a time step of 1 day for the tracer equations and 20 min. for the momentum equations.

Furthermore, we globally balanced the freshwater flux by annually adjusting the precipitation field (Appendix A). We
15   compiled the code using the GNU Fortran compiler gfortran version 5.3.0 and performed the simulation on 6 cores of a processor of type Intel Xeon E5-2630 v3. The simulation was integrated for 3000 years (1000 model years took ~ 7.5 CPU hours) to reach a quasi-steady state, continued for a further 3000 years with stable water isotopes as passive tracers. For analysis the average of the last 100 years was used.

20   **2.2 Implementation of water isotopes**

We implemented the stable water isotopes $H_2^{16}O$, $H_2^{18}O$ and HDO as conservative, passive tracers in the ocean component of the MITgcm. Isotopic variations at the sea surface were driven by evaporation (E), precipitation (P) and river runoff (R), while advection, diffusion and convection affected the distribution in the interior of the ocean. Monthly climatological means of the isotopic content of precipitation and water vapor were available from the National Center for Atmospheric Research
25   Community Atmosphere Model including a water isotope scheme (NCAR IsoCAM – Tharammal et al., 2013). Note that the prescribed atmospheric forcing fields obtained from the PI ocean state estimate by Kurahashi-Nakamura et al., (submitted) and the corresponding isotopic fluxes are not entirely consistent and might introduce an error in our model simulation. However, to minimize the uncertainty we only took the ratio of the isotopic content of precipitation and water vapor and applied it to the corresponding atmospheric forcing fields. The isotopic composition of river runoff affects the isotopic
30   composition of ocean water ($\delta^{18}O_w$ and δD_w) particularly in coastal regions. Since there was no land model in the MITgcm to calculate the amount and isotopic composition of continental runoff, we assumed that it equals the isotopic composition of the local precipitation at the river mouth and again applied it to the runoff forcing field.

Fractionation during evaporation, taking both equilibrium effects and kinetic effects into account, was treated explicitly in the MITgcm. The formulation for the isotopic composition of evaporation E^i [mol m^{-2} s^{-1}] is

$$E^i = \Gamma^i(q^i - q_s^i). \tag{2}$$

Here, q^i is the specific humidity [kg kg^{-1}] multiplied by the isotopic ratio derived from the NCAR IsoCAM and

$$q_s^i = q_s \frac{J^i}{\alpha_{l-v}} \tag{3}$$

is the tracer specific humidity [kg kg^{-1}] in thermodynamic equilibrium with the liquid at the ocean surface (Merlivat and Jouzel, 1979). While

$$q_s = \frac{0.98}{\rho_{air}} q_{sat} \tag{4}$$

is the local sea surface humidity [kg kg^{-1}] with q_{sat} being the saturation specific humidity [kg m^{-3}] and ρ_{air} being the atmospheric density [kg m^{-3}],

$$J^i = \frac{c(i) \cdot M(i)}{c(H_2{}^{16}O) \cdot M(H_2{}^{16}O)} \tag{5}$$

is the local sea surface mass ratio with c being the concentration [mol m^{-3}] and M the molar mass [g mol^{-1}] of the respective stable water isotope. The equilibrium fractionation factor α_{l-v} between liquid water and water vapor has been found empirically as a function of temperature and was given by Majoube (1971):

$$\alpha_{l-v}^{\delta^{18}O} = e^{\frac{1.137}{SST^2} \cdot 10^3 - \frac{0.4156}{SST} - 2.0667 \cdot 10^{-3}} \tag{6}$$

$$\alpha_{l-v}^{\delta D} = e^{\frac{28.844}{SST^2} \cdot 10^3 - \frac{76.248}{SST} - 5.2612 \cdot 10^{-2}} \tag{7}$$

with SST being the sea surface temperature [K].

Due to different molecular diffusivities of the isotopes, kinetic fractionation occurs. The kinetic fractionation factor K depends on wind speed U [m s^{-1}] through the roughness of the air-sea interface (Merlivat and Jouzel 1979; Jouzel et al., 1987):

$$K_{H_2^{18}O} = \begin{cases} 0.006, & if \ U < 7 \ m \ s^{-1} \\ 0.000285 \cdot U + 0.00082, & if \ U \geq 7 \ m \ s^{-1} \end{cases} \tag{8}$$

$$K_{HDO} = \begin{cases} 0.00528, & if \ U < 7 \ m \ s^{-1} \\ 0.0002508 \cdot U + 0.0007216, & if \ U \geq 7 \ m \ s^{-1} \end{cases} \tag{9}$$

The kinetic fractionation factor was used to calculate the isotopic profile coefficient Γ^i following:

$$\Gamma^i = \rho C_E U (1 - K) \tag{10}$$

where ρ is the air density and C_E is the transfer coefficient for evaporation.

Fractionation during the formation of sea ice was neglected, because it is very small compared to other fractionation processes and thus only leads to minor effects on $\delta^{18}O_w$ and δD_w (Craig and Gordon, 1965). Due to the absence of isotopes in the sea ice we approximated the isotopic surface flux F^i [mol m^{-3} s^{-1}] by:

$$F^i = -(E^i - P^i) \cdot (1 - A_{ice}) - R^i \tag{11}$$

with A_{ice} being the ice covered area fraction. Based on this approximation, there was no isotopic surface flux in areas covered by sea ice unless they were influenced by river runoff. Within the MITgcm, processes that affected the stable water isotopes were taken care of by the "gchem" and "ptracers" packages. While the "gchem" package added F^i to the passive tracer surface tendency $gPtr$ [mol m^{-3} s^{-1}]

$$gPtr^i = gPtr^i + F^i,$$ (12)

the "ptracers" package mainly accounted for advection and diffusion of the isotopes. Furthermore, due to the freshwater flux that effectively changed the water column height, an additional tracer flux F_w^i [mol m^{-2} s^{-1}] associated with this input/output of freshwater F_w [kg m^{-2} s^{-1}] was calculated following

$$F_w^i = F_w \cdot c_i \cdot x$$ (13)

with x being an units conversion factor. F_w^i was then additionally added to the tracer surface tendency within the "ptracers" package

$$gPtr^i = gPtr^i + F_w^i \cdot \frac{1}{z}$$ (14)

with z [m] being the surface grid cell thickness.

In the MITgcm, the stable water isotopes were not treated as ratios, but as individual concentrations. Therefore, we initialized the ocean with homogenous concentrations of H$_2^{16}$O, H$_2^{18}$O and HDO matching present-day δ^{18}O$_w$ and δD$_w$ values of 0‰ with reference to the VSMOW. The ratios were calculated during the analysis of the results.

Furthermore, similar to the freshwater flux, a correction factor for the tracer specific precipitation was applied, whereby the respective global tracer concentration in the ocean was conserved (cf. Appendix A).

2.3 Observational data

2.3.1 δ^{18}O$_w$ data

The Goddard Institute for Space Studies (GISS) Global Seawater Oxygen-18 Database v1.21 comprises over 26,000 seawater δ^{18}O values collected since about 1950 (Schmidt et al., 1999) and therefore offers an opportunity to validate the modeled oceanic δ^{18}O values.

For comparison, we interpolated the GISS samples to the nearest tracer grid point of our model grid using inverse distance weighting. We excluded any data point with applied correction, from enclosed lagoons, representing estuarine or river data from near the coast or heavily influenced by meltwater, which means that we rejected all data points flagged as G. H, I, J, L and X in the GISS database (see Schmidt et al., 1999 for details – 23,232 data points remained). We could not expect our model to reproduce such conditions, based on our relatively coarse grid resolution.

Since the GISS data usually represent samples taken at a certain time during the year, we did not compare them to simulated annual mean isotope values. Instead, we used a long-term mean monthly value of the specific month, when the GISS sample was measured.

2.3.2 $\delta^{18}O_c$ data

Waelbroeck et al. (2005) provide a global compilation of $\delta^{18}O_c$ that has been assembled within the Multiproxy Approach for the Reconstruction of the Glacial Ocean surface (MARGO) project. It contains over 2100 core-top and Late Holocene data from planktic foraminifera, mainly measured in *Globigerinoides ruber pink* and *white*, *Globigerina bulloides*, *Neogloboquadrina pachyderma* sinistral and dextral and *Globigerinoides sacculifer* and was used for comparison. The isotopic composition of calcite ($\delta^{18}O_c$) is linked to the temperature T during calcification and the $\delta^{18}O_w$. We used the paleotemperature equation from Mulitza et al. (2004)

$$T\,[°C] = 14.32 - 4.28 \cdot (\delta^{18}O_c - \delta^{18}O_w) + 0.07 \cdot (\delta^{18}O_c - \delta^{18}O_w)^2 \qquad (15)$$

to determine this dependency. Since water samples are reported relative to the VSMOW standard and carbonate samples relative to the Vienna PeeDee Belemnite (VPDB) standard, the $\delta^{18}O_w$ values need to be converted by subtracting -0.27 ‰ (Hut, 1987).

3 Results

3.1 Temperature and salinity distribution at the sea surface

We compare the simulated SST and sea surface salinity (SSS) to the World Ocean Atlas 2013 (WOA13 – Locarnini et al., (2013)), respectively (Fig.1a, b and 2a, b). In most regions of the world ocean, SST differences are around 1 °C or even less (root mean square error (RMSE) = 1.18 °C) and therefore in good agreement with the data. Larger differences are mainly located in regions of coastal and equatorial upwelling, in the Gulf Stream and around Indonesia.

A different picture emerges for the SSS anomaly. While most parts of the surface ocean are slightly too fresh, especially the Mediterranean Sea, Bay of Bengal, Hudson Bay and north of Iceland, both the Arctic Ocean and the east coast of North America are too salty. Nevertheless, we obtain a RMSE of 0.45 psu without using any salinity restoring.

3.2 Stable water isotope distribution in ocean water

In the following, we will only focus on the comparison for $\delta^{18}O$, since the number of measurements for δD is rather small. The surface distribution of $\delta^{18}O_w$ simulated by the MITgcm gradually decreases from the mid-latitudes to high latitudes (Fig. 3a, b). Highest values of about 1 ‰ occur in the subtropical gyre of the Atlantic Ocean, which are slightly higher than in the Pacific Ocean, reflecting the net freshwater transport by the trade winds. The Mediterranean Sea and Red Sea are regions of net evaporation and therefore contain $\delta^{18}O_w$ values of similar magnitude. The most depleted surface water is simulated in the high latitudes, showing values of -0.5 ‰ in the Southern Ocean and -1 ‰ in the Arctic Ocean. These depleted values result from negative $\delta^{18}O_w$ values in precipitation in combination with river/glacial runoff. Similar depleted values occur in surface waters around Indonesia.

The large scale pattern and latitudinal gradients of simulated $\delta^{18}O_w$ values match fairly well the observations. For example, the model captures the contrast between high and low latitudes and the Atlantic and Pacific Ocean. However, some notable discrepancies are recognizable when comparing the absolute range of $\delta^{18}O_w$ at the surface. The subtropical gyres are less enriched in the MITgcm (mean value of 0.6 ‰ as compared to 1.0 ‰, respectively), while $\delta^{18}O_w$ values in the Arctic Ocean

5   are not as depleted as the observational data (mean value -0.6 ‰ as compared to -1.5 ‰, respectively). Especially near large river estuaries, the model-data mismatch is large.

A clear distinction between different water masses based on the isotopic composition of sea water is recognizable in our simulation, both for the Atlantic Ocean and Pacific Ocean (Fig. 4a and 4b respectively). In our model, the North Atlantic Deep Water (NADW) in the Atlantic Ocean reaches down to approximately 3500 m depth and is rather enriched in $H_2^{18}O$,

10   resulting in a $\delta^{18}O_w$ content of around 0.11 ‰ (cf. Table 1). Most enriched $\delta^{18}O_w$ values (~ 0.6 ‰) occur in the upper water column of the tropics (20° - 30 ° S and N). The NADW encounters the Antarctic Intermediate Water (AAIW) coming from the south at a water depth of approximately 1000 m. The latter is more depleted with a $\delta^{18}O_w$ value of around 0 ‰. The deepest parts of the Atlantic Ocean are characterized by negative $\delta^{18}O_w$ values of approximately -0.11 ‰ from the Antarctic Bottom Water (AABW) mixed with NADW. This water mass structure is also recognizable in the observational data and

15   therefore in good agreement. However, the NADW is not enriched enough compared to the observational data (0.21 ‰), whereby the deepest parts of the Atlantic Ocean reveal too depleted $\delta^{18}O_w$ values. For the Pacific Ocean (Fig. 4b) the vertical structure is even more homogenously stratified. Enriched waters (~0.1 ‰) occur in the upper water column down to approximately 1000 m. Deeper parts of the Pacific are filled with depleted water of around -0.1 ‰. Compared to the observational data, the vertical and latitudinal gradients are in agreement. The large number of negative $\delta^{18}O_w$ measurements

20   at 50° N is obtained from the Okhotsk Sea and thus is not representative for the North Pacific.

To take a closer look at the model-data fit, we interpolated the GISS data to the nearest tracer grid point (see section 2.3.1). The separation of the model-data comparison into different ocean basins (Atlantic Ocean - Fig. 5a, Pacific Ocean - Fig. 5b, Arctic Ocean - Fig. 5c and Indian Ocean - Fig. 5d) points to deviations that mainly occur in higher latitudes. The correlation and RMSE is quite diverse, showing strong correlation for the Indian ($r^2 = 0.77$, RMSE = 0.19 ‰) and Pacific Ocean ($r^2 =$

25   0.74, RMSE = 0.32 ‰), medium correlation for the Atlantic Ocean ($r^2 = 0.37$, RMSE = 0.79 ‰) and no correlation for the Arctic Ocean ($r^2 = 0.05$, RMSE = 1.18 ‰). Overall, depleted $\delta^{18}O_w$ values are not very well simulated in the MITgcm, which is particularly recognizable in the Arctic, a region highly influenced by negative $\delta^{18}O_w$ values from river runoff (Yi et al., 2012).

3.3 Stable water isotopes and salinity relation

30   Similar physical processes determine the salinity and $\delta^{18}O_w$ distribution at the ocean surface. Thus locally a linear relationship between those two quantities can be expected. Restricting salinity range to 28 – 38 psu in order to reflect open ocean conditions, the general features of the latter relationship are well captured in our model (Fig. 6).

The modeled $\delta^{18}O_w$-salinity relationship in the tropics agrees quite well with the observed one (Fig. 6a). Here, we find a simulated slope of 0.15 ‰ psu⁻¹, while the observed one is 0.22 ‰ psu⁻¹. A steeper slope is visible in the mid-latitudes for both the simulated and observed relationship (Fig. 6b). However, the agreement between those two slopes slightly decreases, with a simulated slope of 0.28 ‰ psu⁻¹ and an observed slope of 0.49 ‰ psu⁻¹. Further, it underlines that we do not simulate

5   salinity and $\delta^{18}O_w$ values as low as represented in the GISS data.

3.4 $\delta^{18}O_c$ distribution

The simulated $\delta^{18}O_c$ distribution at the surface increases from the tropical regions (~ 3‰) to high latitudes (~ 3.5 ‰), nicely reflecting the dependency on both $\delta^{18}O_w$ and temperature (Fig. 7). Even though most of the observational data is located in the North Atlantic, a latitudinal increase in $\delta^{18}O_c$ is recognizable. Thus the simulated large-scale pattern and latitudinal

10   gradient match fairly well the measurements. Nevertheless, some model-data mismatch occurs. Simulated surface waters around Indonesia are too depleted as well as along coastal upwelling regions and in the Mediterranean Sea. Furthermore, regions in the North Atlantic, which are influenced by the Gulf Stream, are not sufficiently enriched compared to the observations. Overall, the simulated $\delta^{18}O_c$ distribution at the surface tends to be slightly too low. This becomes even clearer when performing a model-data comparison (Fig. 8a) by interpolating the $\delta^{18}O_c$ data to the nearest tracer grid point

15   (analogously to the GISS data). Most of the data points plot below the 1:1 line. The cause for this bias is a matter of investigation and will be discussed in section 4.3. Nevertheless, we get a strong correlation with r² = 0.90 and RMSE = 1.01 ‰.

4 Discussion

4.1 Sources of error

20   Results of the $\delta^{18}O_w$ distribution at the sea surface showed relatively large mismatches in the Arctic Ocean. As indicated by Eq. 11, there is no isotopic surface flux in areas that are covered by sea ice unless they are influenced by river runoff. Since parts of the Arctic Ocean are covered by sea ice all year round and others are seasonally influenced (not shown here), these areas do not experience any isotopic surface flux during most of the year. In this way the impact of precipitation and snow fall that is highly depleted is neglected, which could explain too high $\delta^{18}O_w$ values in the Arctic Ocean. Insufficient river

25   discharge and neglecting the fractionation during sea ice formation could be further sources for the model-data deviations. As part of the Pan-Arctic River Transport of Nutrients, Organic Matter and Suspended Sediments (PARTNERS) project, Cooper et al. (2008) published flow-weighted annual mean $\delta^{18}O_w$ data (collected between 2003 and 2006) from the six largest Arctic rivers. According to their estimates, $\delta^{18}O_w$ values of Eurasian rivers decrease from west-to-east, thus the Ob' river discharges the most enriched freshwater (-14.9 ‰) while the water of the Kolyma river is most depleted in heavy

30   isotopes (-22.2 ‰). This west-to-east trend is also recognizable in our model (Fig. 9), where the Ob' river contributes

freshwater with a $\delta^{18}O_w$ value of around -15.6 ‰ and the Kolyma river of around -20.5 ‰. Even though it seems that the isotopic composition of the Ob' river is overestimated, all the other three rivers are not as depleted as seen in the PARTNERS data.

Measurements of the Yukon and Mackenzie rivers reveal intermediate isotopic signals (-20.2 ‰ and -19.1 ‰ respectively).
5   In the MITgcm these signals are slightly more enriched with $\delta^{18}O_w$ values of around 19.5 ‰ and 18.9 ‰ for the Yukon and Mackenzie rivers respectively. A consideration of the overall river discharge to the Arctic Ocean reveals a slight underestimate as the flow-weighted average for all six rivers is -18.8 ‰, while in the model it is only -17.9 ‰. Therefore, insufficient river runoff could add to the model-data mismatch in the Arctic Ocean. The general pattern of the simulated isotopic river discharge shows that river runoff is more enriched in low and mid-latitudes, which is in accord with
10   observations (IAEA, 2012). Thus, simulating the isotopic composition of river runoff by taking the isotopic composition of the local precipitation is a reasonable first approximation, but should be overcome by implementing a bucket model in the MITgcm, which calculates the river discharge and its isotopic content for individual catchment areas over land.

During the formation of sea ice, the heavier isotopes are entrapped in the solid ice structure, while depleted sea ice brine is expelled (O'Neil, 1968). However, this fractionation process is relatively small. Lehmann and Siegenthaler (1991) reported
15   an equilibrium fractionation constant of $2.91 \cdot 10^{-3}$ between pure water and ice under equilibrium laboratory conditions, while Melling and Moore (1995) estimated a fractionation constant of $2.09 \cdot 10^{-3}$ for ~1 m thick ice in the Canadian Beaufort Sea. So even though sea ice is highly dynamic, since it forms in one location and melts somewhere else, excluding not only the fractionation during the formation of sea ice but also the transportation of isotopes within the sea ice might lead to minor local changes but should not be one of the main sources of error. Indeed, Brennan et al. (2013) investigated the impact of a
20   fractionation factor for sea ice on $\delta^{18}O_w$ within the University of Victoria Earth System Climate Model (UVic ESCM). They conclude that local changes in $\delta^{18}O_w$ due to the contribution of sea ice are smaller than 0.14 ‰ and therefore rather negligible.

Furthermore, the coarse resolution of our model may trigger some of the model-data discrepancies, since it is not able to resolve all of the physical processes. For instance, water that is transported towards the Nordic Seas as parts of the Gulf
25   Stream System is displaced by water from the Labrador Sea due to the coarse grid system. Additionally, our isotopic forcing was not obtained from the same source as the atmospheric forcing for the freshwater, heat and momentum flux, whereby a maximum consistency cannot be ensured and an additional uncertainty to our sources of error is added.

Despite these sources of error, the simulated pattern of $\delta^{18}O_w$ both at the sea surface as well as in the deep ocean agrees fairly well with other recent studies such as the study by Xu et al. (2012) with an OGCM as well as the studies by Roche and Caley
30   (2013) and Werner et al. (2016) with fully coupled models.

4.2 Water mass structure

The seawater oxygen isotope ratio and salinity are controlled by the same processes such as evaporation, precipitation, river runoff and sea ice formation. In this way they are locally linearly related, resulting in a slope that varies between 0.1 ‰ psu^{-1} in low latitudes and up to 1 ‰ psu^{-1} in high latitudes. However, water that is evaporated from the ocean surface does not

5 carry any salt, but stable water isotopes. The agreement between the simulated slope and observational slope in the tropical regions is good, but significantly weaker in the mid-latitudes. This mismatch is rather caused by the stable water isotopes since the overall comparison to observed SSS is quite good. With an RMSE of 0.45 psu our SSS results are comparable to Danabasoglu et al. (2012), who report an RMSE of 0.41 psu for the POP2 ocean component of the Community Climate System Model 4 (CCSM4) using a weak salinity restoring, and Griffies et al. (2011), who got an RMSE of 0.77 with the

10 Geophysical Fluid Dynamics Laboratory Climate Model version 3.

Subtropical gyres are characterized by high salinity and $\delta^{18}O_w$ values. While the model shows reasonable salinities in these regions (Fig. 2a), its surface water is too depleted (Fig. 3a). Either the precipitation is isotopically too depleted or water evaporating from the ocean surface is too enriched, whereby surface water is not enriched enough. As opposed to this are the low salinity and $\delta^{18}O_w$ values at the other end of the slope. Again, simulated salinity values are reasonable, but $\delta^{18}O_w$ values

15 are not as depleted as seen in observations. Since these values are mainly located around the upper boundary of the mid-latitudes (~ 60 °N/S) near the coast, e.g. the Okhotsk Sea and Bering Sea, we infer that the isotopic composition of river runoff is the main driver for this mismatch. Despite these discrepancies at the sea surface, the investigation of the water mass structure of the deeper parts of the ocean reveals that the model is suitable to determine the large scale distribution of water masses in terms of the $\delta^{18}O_w$ signature. Water mass formation regions are mainly located in the high-latitude Atlantic Ocean

20 and produce large parts of the deep and bottom waters of the world ocean. Hence, our investigation focuses on the main water masses (AAIW, AABW and NADW) within that basin. Emery and Meincke (1986) used published temperature and salinity data to determine the core properties of the main water masses of the world ocean. Applying these characteristics of the Atlantic Ocean to both the GISS data and modeled values (Fig. 10; Table 1), clearly shows the resemblance. All three water masses are found in the ocean model, but their temperature-salinity ranges differ slightly from those given by Emery

25 and Meincke (1986). Both, NADW and AABW are slightly saltier in the model, while the AABW also seems to be colder. Nevertheless, even though the absolute range of $\delta^{18}O_w$ values is narrower in the model than in observations, the modeled mean values are remarkably close to observations (cf. Table 1). Our results are quite encouraging, particularly with regard to the nonlinear free surface and real freshwater flux boundary conditions the MITgcm provides and are an improvement compared to other ocean models using salinity restoring (e.g. Paul et al., 1999; Xu et al., 2012).

30 Overall, even though some regions at the surface reveal biased spots regarding the $\delta^{18}O_w$ distribution, the water mass structure of the deeper parts of the ocean and their characteristic $\delta^{18}O_w$ values are successfully simulated. Hence, the ocean model is well suited to perform long-term simulations in a paleoclimatic context and investigating the respective $\delta^{18}O_w$ changes.

4.3 Planktonic foraminiferal $\delta^{18}O_c$

To address questions regarding the evolution and history of the ocean and climate, oxygen isotopic records derived from measurements of foraminiferal shells have been used extensively. Particularly, the last glacial maximum (LGM) and last deglaciation are time periods, for which the evidence comes from proxy data recorded as oxygen isotopes in $CaCO_3$. Hence,

5 before using the model for paleostudies, an evaluation of modeled and measured $\delta^{18}O_c$ for the PI climate is necessary.

Apart from a few data points (red circle – Fig. 8a) most of the modeled $\delta^{18}O_c$ values fall below the 1:1 line and thus are biased towards lower values (Fig. 8a). The outliers are all located in high latitudes in the Arctic Ocean, which is, as mentioned before, a critical area in our model. We checked whether the mismatch is caused by temperature or $\delta^{18}O_w$. The temperature difference between modeled values and the WOA13 for the respective grid cells is rather small (differences not

10 bigger than 0.15 °C) and can be ruled out as the main driving factor for our enriched $\delta^{18}O_c$ values. However, $\delta^{18}O_w$ is mainly increased by more than 1 ‰ and thus certainly leads to increased $\delta^{18}O_c$ values. The reason for the systematic offset of our modeled values is rather a matter of choice of the applied paleotemperature equation. The paleotemperature equation from Mulitza et al. (2004) is derived from plankton-tow specimens. Bé (1980), Duplessy et al. (1981) and Mulitza et al. (2004) as well as others argue that some planktonic foraminifera add an additional layer of calcite during reproduction (gametogenic

15 calcification). This additional calcite layer is secreted in deeper and cooler water masses, introducing an ^{18}O enrichment in the shell. Duplessy et al. (1981) ascertained a $\delta^{18}O$ mean enrichment of 0.78 ‰ and 0.92 ‰ in the shells of *G. ruber* and *G. sacculifer* from core-top sediments, respectively. Mulitza et al. (2004) also showed that foraminiferal shells from the sediment are increased in $\delta^{18}O$ by approximately 0.5-1 ‰. Our systematic offset of 0.74 ‰ falls into the range of these observed values and thus supports the notion that oxygen isotope values from core-top and sediment data are generally much

20 higher than their plankton-tow counterparts. Hence, we assume that the core-top and Late Holocene data contain the signal formed by gametogenic calcification, while our $\delta^{18}O_c$ values calculated with the paleotemperature equation of Mulitza et al. (2004) only represent surface water conditions. Furthermore, one has to keep in mind that we compare modeled annual mean values to measurements of foraminiferal shells that do not represent an annual average but likely contain a seasonal bias, which is not considered (Žarić et al., 2005). Additionally, the isotopic composition of foraminiferal shells can also be altered

25 after deposition due to dissolution. This is especially the case, if the initial shell is dissolved rather than the crust formed during gametogenesis (gametogenic calcite is often more resistant to dissolution (Bé et al., 1975)), further shifting the $\delta^{18}O$ towards higher values.

The observed offset vanishes, when applying the often used paleotemperature equation from Shackleton (1974) to our simulated values and comparing them to the dataset of Waelbroeck et al. (2005) (Fig. 8b). The RMSE slightly improves,

30 while the r² and the slope almost remain unchanged (Table 2). However, this is not surprising, since the equation established by Shackleton (1974) is based on the shells of the benthic foraminifera *Uvigerina spp*, which, according to Zahn et al. (1986), are relatively enriched in ^{18}O. They assume that a low pH and decreased carbonate ion concentration, due to their habitat, might cause this latter enrichment. Based on these outcomes, we suggest, when modeling $\delta^{18}O_c$ of planktonic

foraminifera and their respective surface water conditions, it is more appropriated to use paleotemperature equations derived from plankton-tow data (e.g. Mulitza et al., 2004) or more recent culture experiments (e.g. Spero et al., 2003), particularly since processes that affect the $\delta^{18}O_c$ of core-top sediments (e.g. gametogenic calcification) are not simulated and the commonly used paleotemperature equations like Shackleton (1974) or Kim and O'Neil (1997) tend to overestimate SST.

5   We further checked the agreement between modeled $\delta^{18}O_c$ and a data set derived from plankton tows (Duplessy et al., 1981, Kahn and Williams (1981), Ganssen 1983, Bauch et al., 1997 and Mulitza et al., 2003). Indeed, the MITgcm nicely reflects the $\delta^{18}O_c$ of living specimens (Fig. 8c) with a RMSE of 0.49 ‰ (Table 2). This further supports our assumption that $\delta^{18}O_c$ values from core-top sediments are a mixture of shells calcified at different water depths rather than just a pure surface water signal.

10 We conclude that the modeled $\delta^{18}O_c$ values can be compared to data successfully, although data from core-top data are generally much higher. Nevertheless, the latitudinal gradients of surface waters are well preserved and thus simulating temperature and $\delta^{18}O_w$ simultaneously in an ocean model provides a unique opportunity for questions regarding the climate changes.

5 Conclusions

15 Stable water isotopes have been successfully implemented in the MITgcm, using real freshwater and isotopic flux boundary conditions in conjunction with the non-linear free surface. The model captures well the broad pattern and magnitude of $\delta^{18}O$ in annual mean seawater, reflecting accurately regions of net evaporation. The most enriched surface water occurs in the subtropical gyre of the Atlantic Ocean, while the surface water in the Arctic Ocean is isotopically most depleted. However, the latter ocean basin is the one with largest model-data discrepancies. They mostly result from a combination of sources of

20 error such as the absence of highly depleted precipitation and snow fall in areas covered by sea ice as well as insufficient river runoff, which is simulated by using the isotopic composition of the local precipitation at the river mouth, but are also attributable to the coarse resolution of the model. The simulated $\delta^{18}O_w$-salinity relationship is in good agreement with observations in tropical regions but less so in mid-latitudes, due to misrepresentation of $\delta^{18}O_w$. But even though the $\delta^{18}O_w$ distribution at the sea surface reveals some deviations, the water mass structure of the deeper parts of the ocean and their

25 characteristic $\delta^{18}O_w$ values are remarkably well captured in our model and show that $\delta^{18}O_w$ indeed can be used to characterize different water masses. Further, we tested simulated $\delta^{18}O_c$ against measurements of planktonic foraminiferal shells. Again, the latitudinal gradients and large-scale patterns are faithfully reproduced. However, we observed a systematic offset towards lower values in our modeled $\delta^{18}O_c$. Gametogenic calcification probably causes this offset, since it is recorded in core-top and Late Holocene data but does not apply to living foraminiferal shells and their respective sea surface conditions. Hence, we

30 suggest it is more appropriated to use paleotemperature equations derived from plankton-tow data or more recent culture experiments to investigate the $\delta^{18}O_c$ of planktonic foraminifera. Furthermore, for a better understanding about the factors that

determine the incorporation of oxygen isotopes in foraminiferal shells, as well as their life cycle, ecosystem models like the one from Fraile et al. (2008) or Kretschmer et al. (2016) are needed.

The MITgcm and its newly developed stable water isotope package offer a great opportunity to perform long-term simulations in a paleoclimatic context and assimilating water isotopes with the adjoint method. Thus, investigations of not only the respective changes in $\delta^{18}O_w$ but also in foraminiferal $\delta^{18}O_c$ during the LGM or last deglaciation can be performed.

6 Code availability

The water isotope package incorporated in the MITgcm can be obtained by contacting the first author: R. Völpel (rvoelpel@marum.de). Additionally, a release of the package through the MITgcm repository will be prepared.

Appendix A

The MITgcm provides a scheme that balances the freshwater flux (net fluxes are set to zero) at each time step, preventing uncontrolled drifts in salinity and sea surface height caused by an imbalance in precipitation, evaporation and runoff. However, this scheme adversely affects the seasonality of the net surface freshwater flux.

Following Large et al. (1997), a precipitation correction factor $f_P(y)$ is implemented in the MITgcm and computed each year y, whereby the global freshwater flux is annually balanced.

The correction factor is applied to the precipitation field, such that the precipitation throughout a model year y is given by:

$$P = f_P(y) \cdot P(y) \qquad\qquad A(1)$$

The size of f_P depends on the change in volume of global ocean freshwater throughout a year (ΔV^F_y) and the volume of precipitation (falling on the ice-free ocean) and river runoff as an annual integral (V^P and V^R, respectively). These values are used to compute the correction factor for the following year:

$$f_P(y+1) = f_P(y)\left(1 - \frac{\Delta V^F_y}{(V^P + V^R)}\right) \qquad\qquad A(2)$$

If the change in volume of global ocean freshwater is positive (negative), the global salinity will decrease (increase) and the correction factor is decreased (increased) for the next year $y+1$. Throughout the model integration changes are getting smaller resulting in a precipitation correction factor that remains approximately constant at $f_P(y) = 1.0014$ after 1500 model years (Fig. A1).

Acknowledgments.

We would like to thank T. Tharammal for providing the isotopic data of NCAR IsoCAM and T. Kurahashi-Nakamura for providing the atmospheric forcing fields obtained with the adjoint model. Further, we would like to thank Martin Losch for

his advice throughout the model development. This project was funded through the DFG Research Center/Center of Excellence MARUM – "The Ocean in the Earth System".

References

Adcroft, A., Hill, C., and Marshall, J.: Representation of topography by shaved cells in a height coordinate ocean model, Mon.Weather Rev., 125, 2293-2315, 1997.

Adcroft, A. and Campin, J.-M.: Rescaled height coordinates for accurate representation of free-surface flows in ocean circulation models, Ocean Model., 7, 269 - 284, doi:10.1016/j.ocemod.2003.09.003, 2004.

Adcroft, A., Campin, J.-M., Hill, C., and Marshall, J.: Implementation of an Atmosphere Ocean General Circulation Model on the Expanded Spherical Cube, Mon. Weather Rev., 132, 2845-2863, doi:10.1175/MWR2823.1, 2004a.

Adcroft, A., Hill, C., Campin, J., Marshall, J., and Heimbach, P.: Overview of the formulation and numerics of the MIT GCM, in: Proceedings of the ECMWF Seminar Series on Numerical Methods: Recent Developments in Numerical Methods for Atmosphere and Ocean Modelling, ECMWF, 139-149, 2004b.

Baertschi, P.: Absolute ^{18}O content of standard mean ocean water, Earth Planet. Sc. Lett., 31, 341-344, doi:10.1016/0012-821X(76)90115-1, 1976.

Bauch, D., Carstens, J., and Wefer, G.: Oxygen isotope composition of living *Neogloboquadrina pachyderma* (sin.) in the Arctic Ocean, Earth Planet. Sc. Lett., 146, 47-58, doi:10.1016/S0012-821X(96)00211-7, 1997.

Bé, A. W. H.: Gametogenic calcification in a spinose planktonic foraminifer, *Globigerinoides sacculifer* (Brady), Mar. Micropaleontol., 5, 283-310, doi:10.1016/0377-8398(80)90014-6, 1980.

Bé, A. W. H., Morse, J. W., and Harrison, S. M.: Progressive dissolution and ultrastructural breakdown of planktonic foraminifera, in: Dissolution of Deep Sea Carbonates, edited by: Sliter, W. V., Bé, A. W. H., and Berger, W. H., Cushman Foundation for Foraminiferal Research, Special Publication, 13, 27-55, 1975.

Brennan, C. E., Meissner, K. J., Eby, M., Hillaire-Marcel, C., and Weaver, A. J.: Impact of sea ice variability on the oxygen isotope content of seawater under glacial and interglacial conditions, Paleoceanography, 28, 388-400, doi:10.1002/palo20036, 2013.

Cooper, L.W., McClelland, J. W., Holmes, R. M., Raymond, P. A., Gibson, J. J., Guay, G. K., and Peterson, B. J.: Flow-weighted values of runoff tracers (δ^{18}O, DOC, BA, alkalinity) from the six largest Arctic rivers, Geophys. Res. Lett., 35, L18606, doi:10.1029/2008GL035007, 2008.

Craig, H. and Gordon, L. I.: Deuterium and oxygen 18 variations in the ocean and the marine atmosphere, edited by: Tongiogi, El., Consiglio nazionale delle richerche, Laboratorio de geologia nucleare, Spoleto, Italy, 9-130, 1965.

Danabasoglu, G., Bates, S. C., Briegleb, B. P., Jayne, S. R., Jochum, M., Large, W. G., Peacock, S., and Yeager, S.G.: The CCSM4 Ocean Component, J. Climate, 25, 1361-1389, doi:10.1175/JCLI-D-11-00091.1, 2012.Fleitmann, D., Burns, S. J.,

Mudelsee, M., Neff, U., Kramers, J., Mangini, A., and Matter, A.: Holocene Forcing of the Indian Monsoon Recorded in a Stalagmite from Southern Oman, Science, 300, 1737-1739, doi:10.1126/science.1083130, 2003.

de Wit, J. C., VanderStraaten, C. M., and Mook, W. G.: Determination of the absolute hydrogen isotopic ratio of V–SMOW and SLAP, Geostandard. Newslett., 4, 33-36, doi:10.1111/j.1751-908X.1980.tb00270.x, 1980.

5   Duplessy, J. C., Blanc, P. L., and Bé, A. W. H.: Oxygen-18 enrichment of planktonic foraminifera due to gametogenic calcification below the euphotic zone, Science, 213, 1247-1250, doi:10.1126/science.213.4513.1247, 1981.

Emery, W. J. and Meincke, J.: Global water masses: summary and review, Oceanol Acta, 9, 383-391, 1986.

Emiliani, C.: Pleistocene temperatures, J. Geol., 63, 538-578, 1955.

Errico, R. M.: What Is an Adjoint Model?, B. Am. Meteorol. Soc., 78, 2577-2591, doi:10.1175/1520-
10   0477(1997)078<2577:WIAAM>2.0.CO;2, 1997.

Fraile, I., Schulz, M., Mulitza, S., and Kucera, M.: Predicting the global distribution of planktonic foraminifera using a dynamic ecosystem model, Biogeosciense, 5, 891-911, doi:10.5194/bg-5-891-2008, 2008.

Ganssen, G.: Dokumentation von küstennahem Auftrieb anhand stabiler Isotope in rezenten Foraminiferen vor Nordwest-Afrika, "Meteor"-Forschungsergebnisse 37C, 1-46, 1983.

15   Gat, J. R. and Gonfiantini, R. (Eds): Stable isotope hydrology: Deuterium and Oxygen-18 in the water cycle, Int. At. Energy Agency, Vienna, 1981.

Gent, P. R. and McWilliams, J. C.: Isopycnal Mixing in Ocean Circulation Models, J. Phys. Oceanogr., 20, 150-160, doi:10.1175/1520-0485(1990)020<0150:IMIOCM>2.0.CO;2, 1990.

Griffies, S. M., Biastoch, A., Böning, C., Bryan, F., Danabasoglu, G., Chassignet, E. P., England, M. H., Gerdes, R., Haak,
20   H., Hallberg, R. W., Hazeleger, W., Jungclaus, J., Large, W. G., Madec, G., Pirani, A., Samuels, B. L., Scheinert, M., Gupta, A. S., Severijns, C. A., Simmons, H. L., Treguier, A. M., Winton, M., Yeager, S., and Yin J.: Coordinated Ocean-ice Reference Experiments (COREs), Ocean Model., 26, 1-46, doi:10.1016/j.ocemod.2008.08.007, 2009.

Griffies, S. M., Winton, M., Donner, L. J., Horowitz, L. W., Downes, S. M., Farneti, R., Gnanadesikan, A., Hurlin, W. J., Lee, H.-C., Liang, Z., Palter, J. B., Samuels, B. L., Witternberg, A. T., Wyman, B. L., Yin, J., and Zadeh, N.: The GFDL
25   CM3 Coupled Climate Model: Characteristics of the Ocean and Sea Ice Simulations, J. Climate, 24, 3520-3544, doi:10.1175/2011JCLI3964.1, 2011.

Huang, R. X.: Real freshwater flux as a natural boundary condition for the salinity balance and thermohaline circulation forced by evaporation and precipitation, J. Phys. Oceanogr., 23, 2428-2446, 1993.

Hundsdorfer, W. and Trompert, R. A.: Method of lines and direct discretization: a comparison for linear advection, Appl.
30   Numer. Math., 13, 469-490, 1994.

Hut, G.: Stable Isotope Reference Samples for Geochemical and Hydrological Investigations. Consultant Group Meeting IAEA, Vienna, 16-18 September 1985, Report to the Director General, Internatinal Atomic Energy Agency, Vienna, Austria, 1987.

IAEA: Global Network of Isotopes in Rivers, available at: http://www-naweb.iaea.org/napc/ih/IHS_resources_gnir.html (last access: 31 August 2016), 2012.

Jackett, D. R. and McDougall, T. J.: Minimal adjustment of hydrographic profiles to achieve static stability, J. Atmos. Ocean. Tech., 12, 381-389, doi:10.1175/1520-0426(1995)012<0381:MAOHPT>2.0.CO;2, 1995.

Jacobs, S. S., Fairbanks, R. G., and Horibe, Y.: Origin and evolution of water masses near the Antarctic continental margin: Evidence from $H_2^{18}O/H_2^{16}O$ ratios in seawater, in: Oceanology of the Antarctic Continental Shelf edited by: Jacobs, S. S., vol. 43 of Antarctic Res. Ser., 59-85, AGU, Washington, D.C., doi:10.1029/AR043p0059, 1985.

Johnsen, S. J., Dahl-Jensen, D., Gundestrup, N., Steffensen, J. P., Clausen, H. B., Miller, H., Masson-Delmotte, V., Sveinbjornsdottir, A. E., and White, J.: Oxygen isotope and palaeotemperature records from six Greenland ice-core stations: Camp Century, Dye-3, GRIP, GISP2, Renland and NorthGRIP, J. Quaternary Sci., 16, 299-307, doi:10.1002/jqs.622, 2001.

Joussaume, S., Sadourny, R., and Jouzel, J.: A general circulation model of water isotope cycles in the atmosphere, Nature, 311, 24-29, doi:10.1038/311024a0, 1984.

Jouzel, J., Russell, G. L., Suozzo, R. J., Koster, R. D., White, J. W. C., and Broecker, W. S.: Simulations of the HDO and $H_2^{18}O$ atmospheric cycles using the NASA GISS general circulation model: the seasonal cycle for present-day conditions, J. Geophys. Res., 92, 14739-14760, doi:10.1029/JD092iD12p14739, 1987.

Kahn, M. and Williams, D. F.: Oxygen and carbon isotopic composition of living planktonic foraminifera from the northeast Pacific Ocean, Palaeogeogr. Palaeocl., 33, 47-69, doi:10.1016/0031-0182(81)90032-8, 1981.

Khatiwala, S. P., Fairbanks, R. G., and Houghton, R. W.: Freshwater sources to the coastal ocean off northeastern North America: Evidence from $H_2^{18}O/H_2^{16}O$, J. Geophys. Res., 104, 18,241-18,255, doi:10.1029/1999JC900155, 1999.

Kim, S. T. and O'Neil, J. R.: Equilibrium and nonequilibrium oxygen isotope effects in synthetic carbonates, Geochim. Cosmochim. Ac., 61, 3461-3475, 1997.

Kretschmer, K., Kucera, M., and Schulz, M..: Modeling the distribution and seasonality of *Neogloboquadrina pachyderma* in the North Atlantic Ocean during Heinrich Stadial 1, Paleoceanography, 31, 986-1010, doi:10.1002/2015PA002819, 2016.

Kurahashi-Nakamura, T., Paul, A., and Losch, M.: Dynamical reconstruction of the global ocean state during the Last Glacial Maximum, submitted to Paleoceanography, 2016.

Large, W. G., Danabasoglu, G., Doney, S. C., and McWilliams, J. C.: Sensitivity to surface forcing and boundary layer mixing in a global ocean model: Annual-mean climatology, J. Phys. Oceanogr., 27, 2418-2447, doi:10.1175/1520-0485(1997)027<2418:STSFAB>2.0.CO;2, 1997.

Large, W. G. and Yeager, S. G.: Diurnal to decadal global forcing for ocean and sea-ice models: The data sets and flux climatologies, NCAR Technical Note, 4-15, doi:10.5065/D6KK98Q6, 2004.

Lehmann, M. and Siegenthaler, U.: Equilibrium oxygen- and hydrogen-isotope fractionation between ice and water, J. Glaciol., 37, 23-26, 1991.

Levitus, S. and Boyer, T.: World Ocean Atlas 1994, Vol. 4: Temperature, NOAA Atlas NESDIS 4, 1994.

Levitus, S., Burgett, R., and Boyer, T.: World Ocean Atlas 1994, Vol. 3: Salinity, NOAA Atlas NESDIS 3, 1994.

Locarnini, R. A., Mishonov, A. V., Antonov, J. I., Boyer, T. P., Garcia, H. E., Baranova, O. K., Zweng, M. M., Paver, C. R., Reagan, J. R., Johnson, D. R., Hamilton, M. and Seidov, D.; World Ocean Atlas 2013, Volume 1: Temperature, edited by: Levitus, S., technical edited by: Mishonov, A., NOAA Atlas NESDIS 73, 40 pp., 2013.

Losch, M., Menemenlis, D., Campin, J.-M., Heimbach, P., and Hill, C.: On the formulation of sea-ice models. Part 1: Effects
5   of different solver implementations and parameterizations, Ocean Model., 33, 129-144, doi:10.1016/j.ocemod.2009.12.008, 2010.

Majoube, M.: Fractionnement en oxygèn 18 et en deutérium entre l'eau et sa vapeur, Journal de Chimie et de Physique 68, 1423-1436, 1971.

Marshall, J., Adcroft, A., Hill, C., Perelman, L., and Heisey, C.: A finite-volume, incompressible Navier Stokes model for
10   studies of the ocean on parallel computers, J. Geophys. Res., 102, 5753-5766, doi:10.1029/96JC02775, 1997.

Melling, H. and Moore, R. M.: Modification of halocline source waters during freezing on the Beaufort Sea shelf: evidence from oxygen isotopes and dissolved nutrients, Continent. Shelf Res., 15, 89-113, doi:10.1016/0278-4343(94)P1814-R, 1995.

Meredith, M. P., Heywood, K. J., Frew, R. D. and Dennis, P. F.: Formation and circulation of the water masses between the Southern Indian Ocean and Antarctica: Results from δ^{18}O, J. Mar. Res., 57, 449-470, 1999.

15   Merlivat, L. and Jouzel, J.: Global climatic interpretation of the deuterium-oxygen 18 relationship for precipitation, J. Geophys. Res., 84, 5029-5033, doi:10.1029/JC084iC08p05029, 1979.

Mulitzy, S., Boltovskoy, D., Donner, D., Meggers, H., Paul, A., and Wefer, G.: Temperature: δ^{18}O relationships of planktic foraminifera collected from surface waters, Palaeogeogr. Palaeocl., 202, 143-152, doi:10.1016/S0031-0182(03)00633-3, 2003.

20   Mulitza, S., Donner, B., Fischer, G., Paul, A., Pätzold, J., Rühlemann, C., and Segl, M.: The South Atlantic oxygen-isotope record of planktic foraminifera, in: The South Atlantic in the Late Quaternary: Reconstruction of Mass Budget and Current Systems edited by Fischer, G. and Wefer, G., 121-142, Springer, New York, 2004.

O'Neil, J. R.: Hydrogen and oxygen isotopic fractionation between ice and water, J. Phys. Chem., 72, 3683-3684, doi:10.1021/j100856a060, 1986.

25   Paul, A., Mulitza, S., Pätzold, J., and Wolff, T.: Simulation of oxygen isotopes in a global ocean model, in: Use of proxies in paleoceanography: examples from the South Atlantic, edited by: Fisher, G. and Wefer, G., 655-686, Springer, Berlin, Heidelberg, Germany, 1999.

Redi, M. H.: Oceanic Isopycnal Mixing by Coordinate Rotation, J. Phys. Oceanogr., 12, 1154-1158, doi:10.1175/1520-0485(1982)012<1154:OIMBCR>2.0.CO;2, 1982.

30   Roche, D. M. and Caley, T.: δ^{18}O water isotope in the *i*LOVECLIM model (version 1.0) – Part 2: Evaluation of the model results against observed δ^{18}O in water samples, Geosci. Model Dev., 6, 1493-1504, doi:10.5194/gmd-6-1493-2013, 2013.

Rohling, E. J. and Bigg, G. R.: Paleosalinity and δ^{18}O: a critical assessment, J. Geophys. Res., 103, 1307-1318, doi:10.1029/97JC01047, 1998.

Schmidt, G. A.: Oxygen-18 variations in a global ocean model, Geophys. Res. Lett., 25, 1201-1204, doi:10.1029/98GL50866, 1998.

Schmidt, G. A., BiggnG. R., and Rohling E. J.: Global seawater oxygen-18 database, available at: http://data.giss.nasa.gov/o18data (last access: 08 July 2016), 1999.

5 Shackleton, N. J.: Attainment of isotopic equilibrium between ocean water and the benthonic foraminifera genus Uvigerina: isotopic changes in the ocean during the last glacial, Gif-sur-Yvette, Colloque international du CNRS, 219, 203-210, 1974.

Spero, H. J., Mielke, K. M., Kalve, E. M., Lea, D. W., and Pak, D. K.: Multispecies approach to reconstructing eastern equatorial Pacific thermocline hydrography during the past 360 kyr, Paleoceanography, 18, 1022,

10 doi:10.1029/2002PA000814, 2003.

Tharammal, T., Paul, A., Merkel, U., and Noone, D.: Influence of Last Glacial Maximum boundary conditions on the global water isotope distribution in an atmospheric general circulation model, Clim. Past, 9, 789-809, doi:10.5194/cp-9-789-2013, 2013.

Wadley, M. R., Bigg, G. R., Rohling, E. J., and Payne, A. J.: On modelling present-day and last glacial maximum oceanic

15 δ^{18}O distributions, Global Planet. Change, 32, 89-109, doi:10.1016/S0921-8181(01)00084-4, 2002.

Waelbroeck, C., Mulitza, S., Spero, H., Dokken, T., Kiefer, T., and Cortijo, E.: A global compilation of Late Holocene planktic foraminiferal δ^{18}O: Relationship between surface water temperature and δ^{18}O, Quaternary Sci. Rev. 24, 853-878, doi:10.1016/j.quascirev.2003.10.014, 2005.

Werner, M., Haese, B., Xu, X., Zhang, X., Butzin, M., and Lohmann, G.: Glacial-interglacial changes in H_2^{18}O, HDO and

20 deuterium excess – results frm the fully coupled ECHAM5/MPI-OM Earth system model, Geosci. Model Dev., 9, 647-670, doi:10.5194/gmd-9-647-2016, 2016.

Xu, X., Werner, M., Butzin, M., and Lohmann, G.: Water isotope variations in the global ocean model MPI-OM, Geosci. Model Dev., 5, 809-818,, doi:10.5194/gmd-5-809-2012, 2012.

Yi, Y., Gibson, J. J., Cooper, L. W., Helie, J.-F., Birks, S. J., Mccleland, J. W., Holmes, R. M., and Peterson, B. J.: Isotopic

25 signals (^{18}O, ^{2}H, ^{3}H) of six major rivers draining the pam-Arctic watershed, Global Biogeochem. Cy., 26, GB1027, doi:10.1029/2011GB004159, 2012.

Zahn, R., Winn, K., and Sarnthein, M.: Benthic foraminiferal δ13C and accumulation rates of organic carbon: *Uvigerina peregrina* group and *Cibicidoides wuellerstorfi*, Paleoceanography, 1, 27-42, 1986.

Žarić, S., Donner, B., Fischer, G., Mulitza, S., and Wefer, G.: Sensitivity of planktic foraminifera to sea surface temperature

30 and export production as derived from sediment trap data, Mar. Micropaleontol., 55, 75-105, doi:10.1016/j.marmicro.2005.01.002, 2005.

Table 1: $\delta^{18}O_w$ characteristics of the main water masses (Antarctic Intermediate Water – AAIW, North Atlantic Deep Water – NADW and Antarctic Bottom Water – AABW) in the Atlantic Ocean for the observational (GISS) and simulated data (MIT).

	AAIW	NADW	AABW
$\delta^{18}O_w^{GISS}$ range [‰]	-2.50 – 1.41	-0.49 – 0.88	-0.31 – 0.00
$\delta^{18}O_w^{GISS}$ mean value [‰]	-0.09	0.21	-0.14
$\delta^{18}O_w^{GISS}$ standard deviation [‰]	0.42	0.09	0.08
$\delta^{18}O_w^{MIT}$ range [‰]	-0.25 – 0.10	0.02 – 0.14	-0.16 – -0.03
$\delta^{18}O_w^{MIT}$ mean value [‰]	0.00	0.11	-0.11
$\delta^{18}O_w^{MIT}$ standard deviation [‰]	0.07	0.03	0.06

5   **Table 2: Data-model comparison of $\delta^{18}O_c$ of planktonic foraminiferas using different palaeotenperature equations (Mulitza et al. (2004) and Shackleton (1974)) and data sets (core-top and Late Holocene (LH) data (Waelbroeck et al., 2005) and living specimens (Duplessy et al., 1981, Kahn ans Williams (1981), Ganssen 1983, Bauch et al., 1997 and Mulitza et al., 2003)).**

Data set	Palaeotemperature equation	RMSE [‰]	r^2	slope [‰ ‰$^{-1}$]
Core-top and LH data	$T\,[°C] = 14.32 - 4.28 \cdot (\delta^{18}O_c - \delta^{18}O_w) + 0.07 \cdot (\delta^{18}O_c - \delta^{18}O_w)^2$ (Mulitza et al., 2004)	1.01	0.9	1.03
Core-top and LH data	$T\,[°C] = 16.90 - 4.38 \cdot (\delta^{18}O_c - \delta^{18}O_w) + 0.01 \cdot (\delta^{18}O_c - \delta^{18}O_w)^2$ (Shackleton, 1974)	0.70	0.9	1.04
Living specimens	$T\,[°C] = 14.32 - 4.28 \cdot (\delta^{18}O_c - \delta^{18}O_w) + 0.07 \cdot (\delta^{18}O_c - \delta^{18}O_w)^2$ (Mulitza et al., 2004)	0.49	0.93	1.06
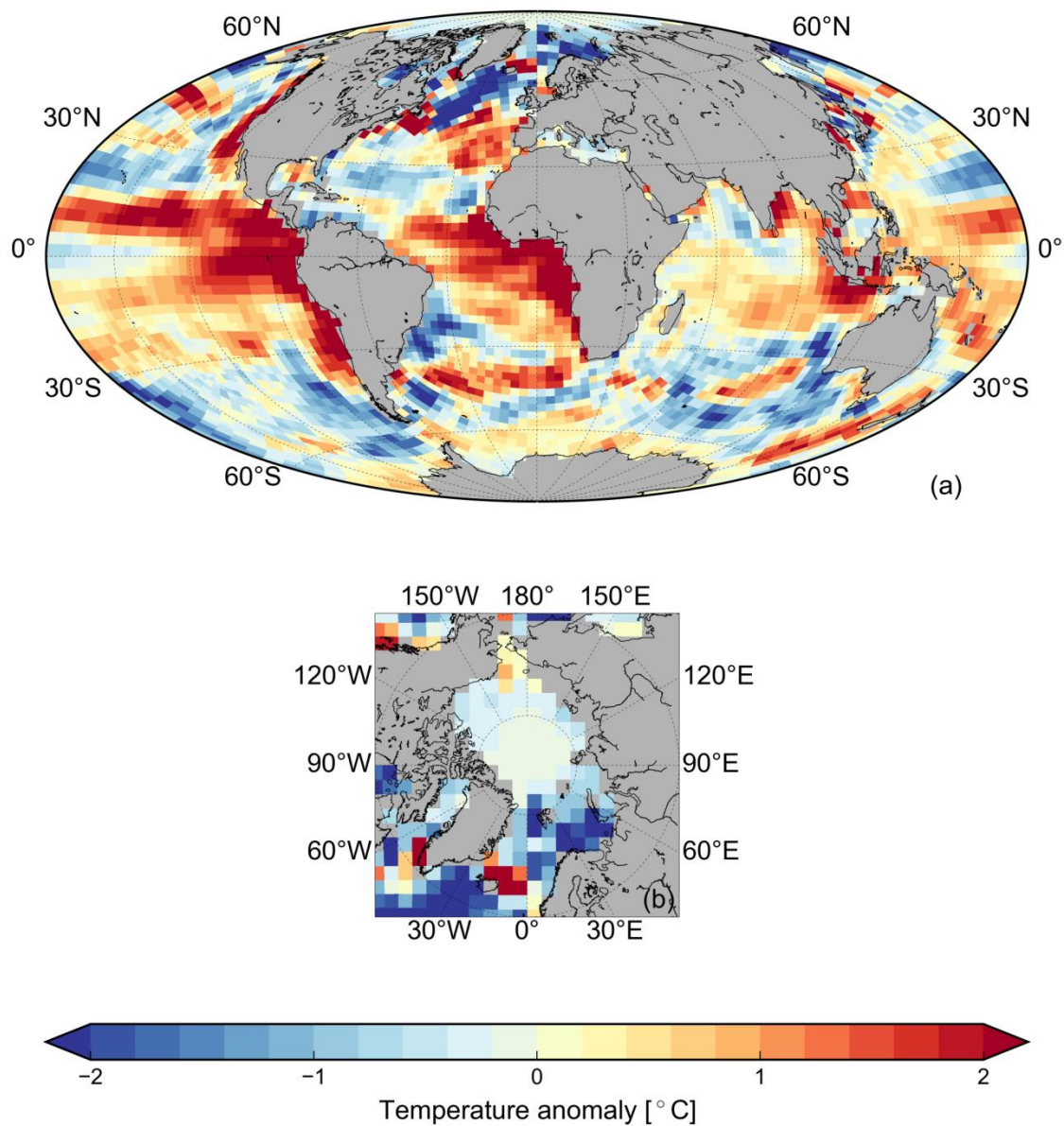
Figure 1: Sea surface temperature anomaly (simulated in the MITgcm – WOA13) for (a) the global ocean and (b) the Arctic Ocean.
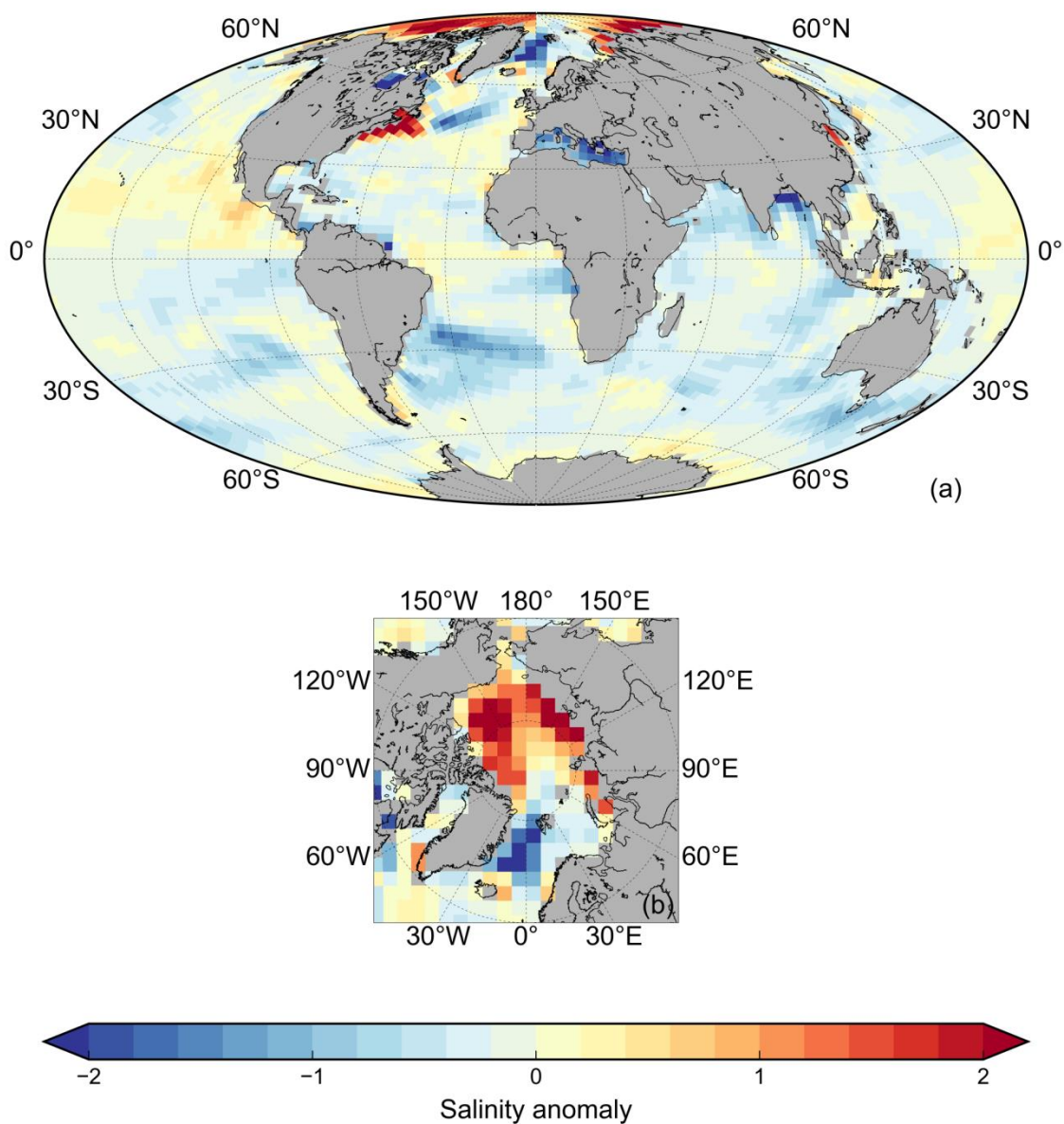
Figure 2: Sea surface salinity anomaly (simulated in the MITgcm – WOA13) for (a) the global ocean and (b) the Arctic Ocean.
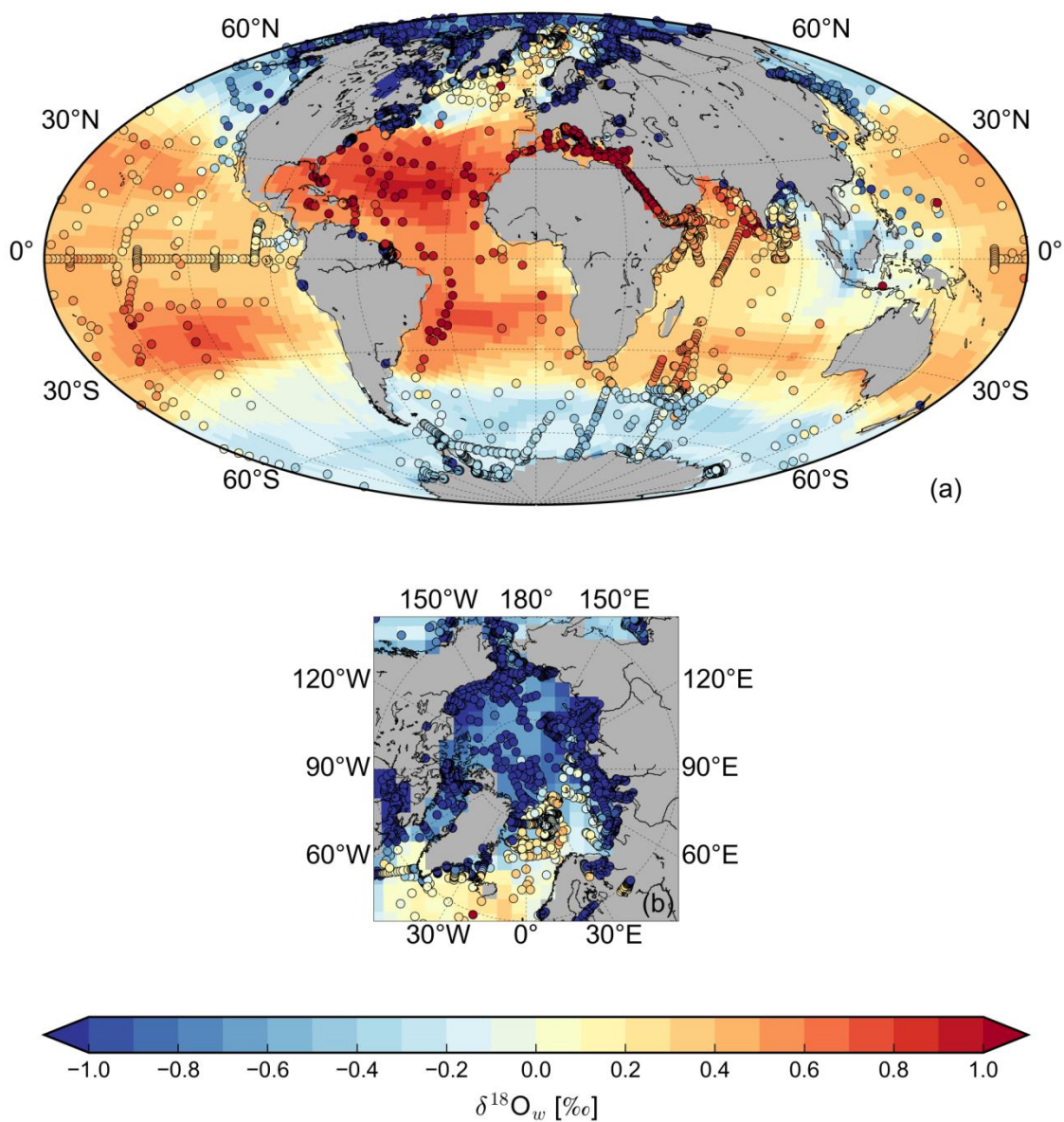
Figure 3: Global surface δ¹⁸O_w distribution simulated by the MITgcm in comparison to the observational GISS data (colored symbols (Schmidt et al., 1999) – averaged over the upper 50 m) for (a) the global ocean and (b) the Arctic Ocean.
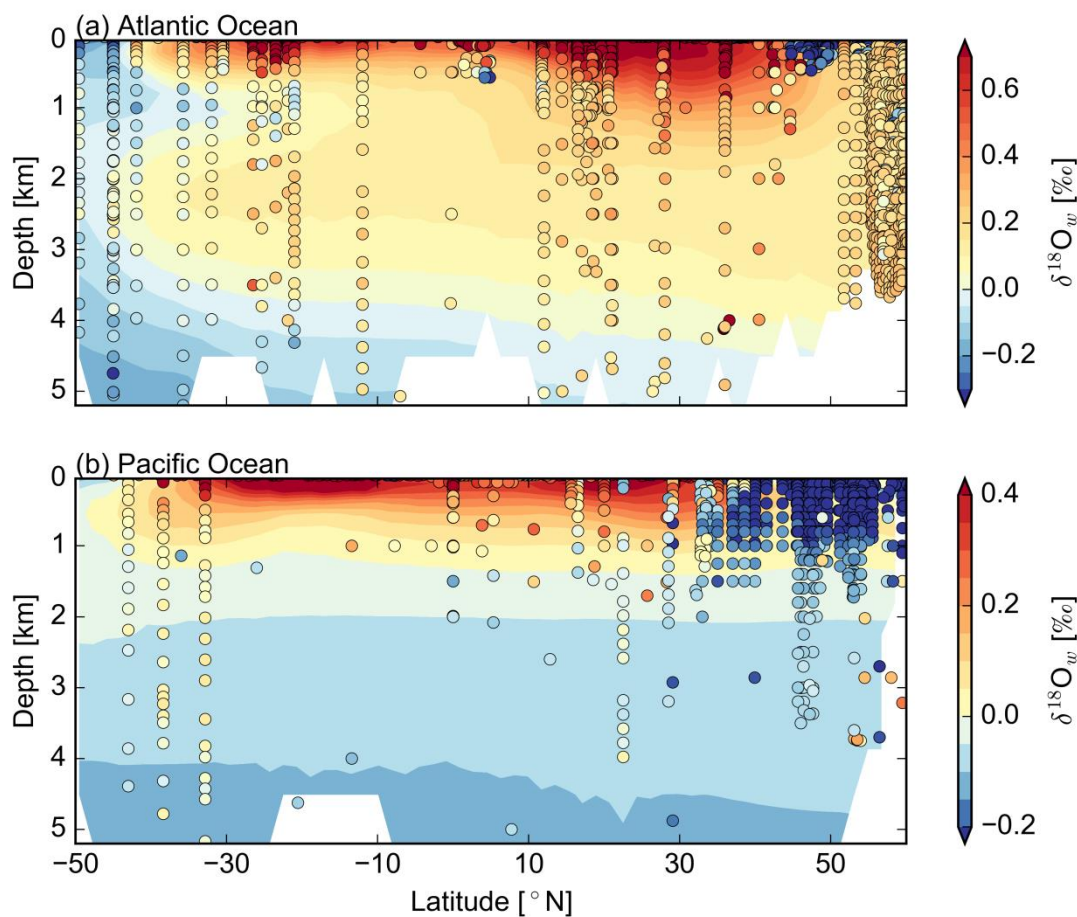
Figure 4: Zonally-averaged cross section for the simulated $\delta^{18}O_w$ distribution in (a) the Atlantic and (b) the Pacific Ocean in comparison to the observational GISS data (colored symbols – Schmidt et al., 1999). Note that the GISS data does not represent a zonal mean, but rather values from specific locations.
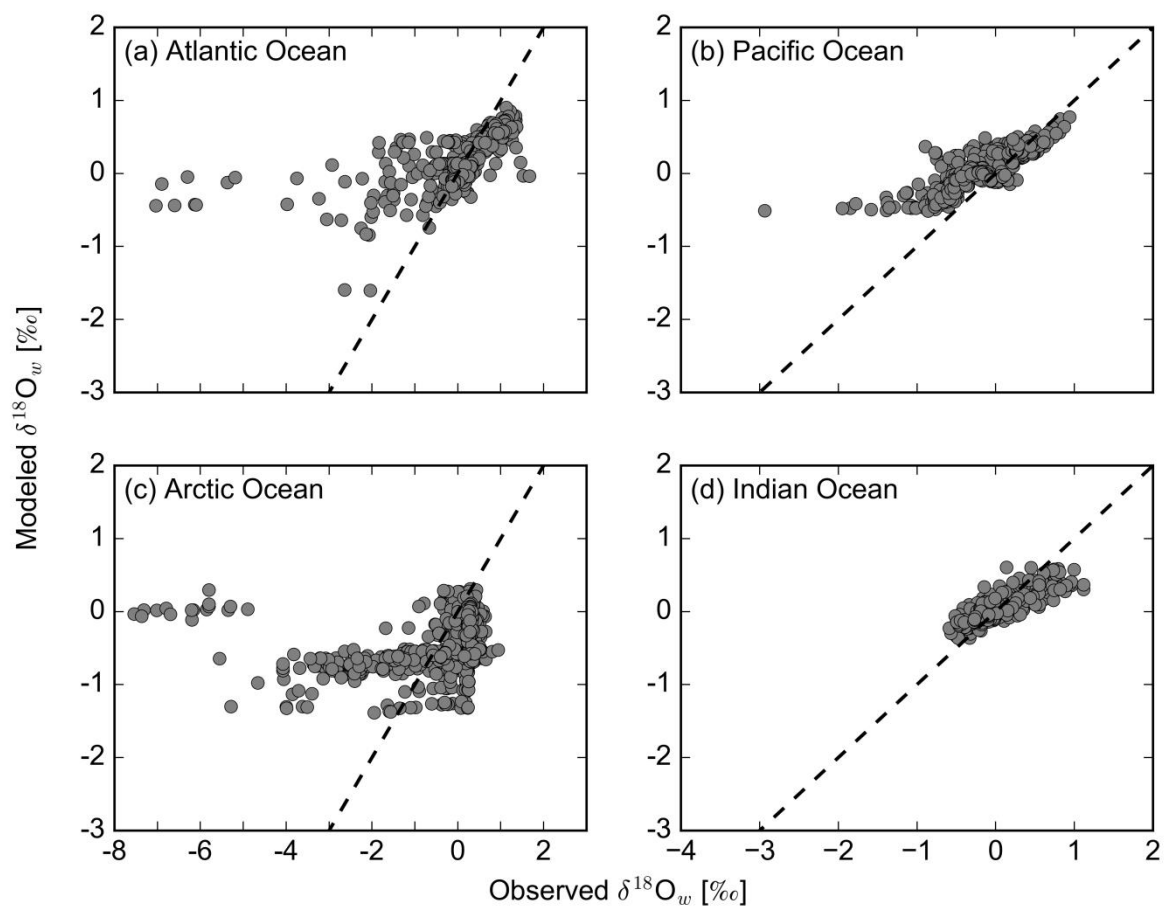
Figure 5: Relationship between observed δ^{18}O$_w$ from the GISS database (Schmidt et al., 1999) and simulated δ^{18}O$_w$ from the MITgcm for the different ocean basins: (a) Atlantic Ocean, (b) Pacific Ocean, (c) Arctic Ocean and (d) Indian Ocean. Dashed lines represent the 1:1 line.
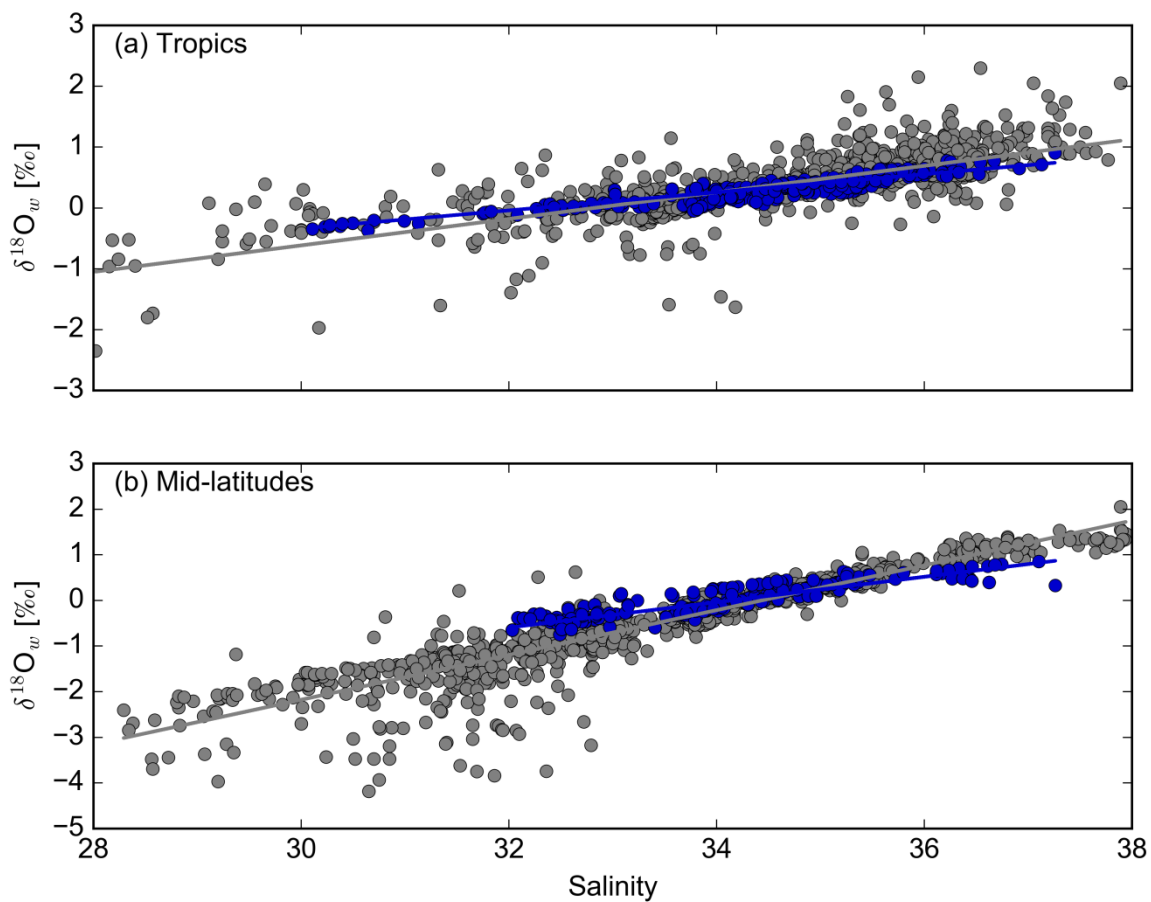
Figure 6: Salinity and $\delta^{18}O_w$ relation in surface waters (50 m) for observational data (grey symbols – Schmidt et al., 1999) and simulated values (blue symbols) in (a) the tropics (25°S – 25°N) and (b) the mid-latitudes (25°S/N – 60°S/N). The $\delta^{18}O_w$/salinity slopes are given in the text.
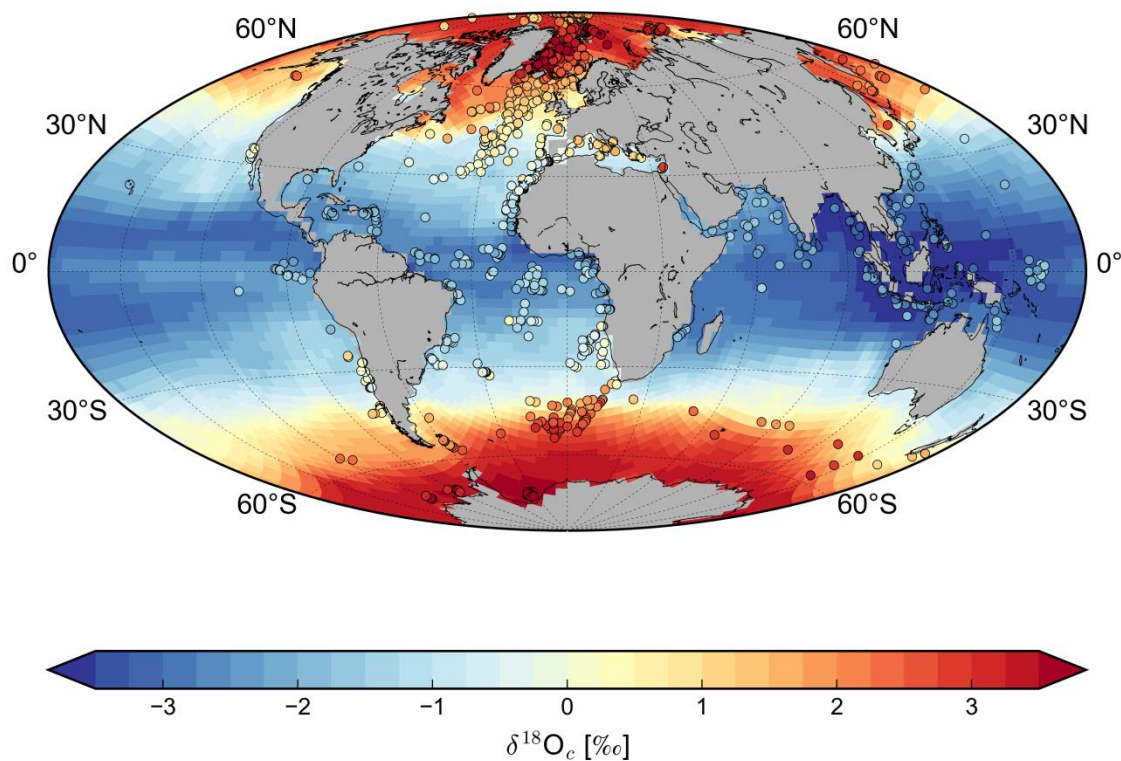
Figure 7: Modeled sea surface $\delta^{18}O_c$ distribution compared to core-top and Late Holocene $\delta^{18}O_c$ from various planktonic foraminiferas (colored symbols - Waelbroeck et al., 2005).
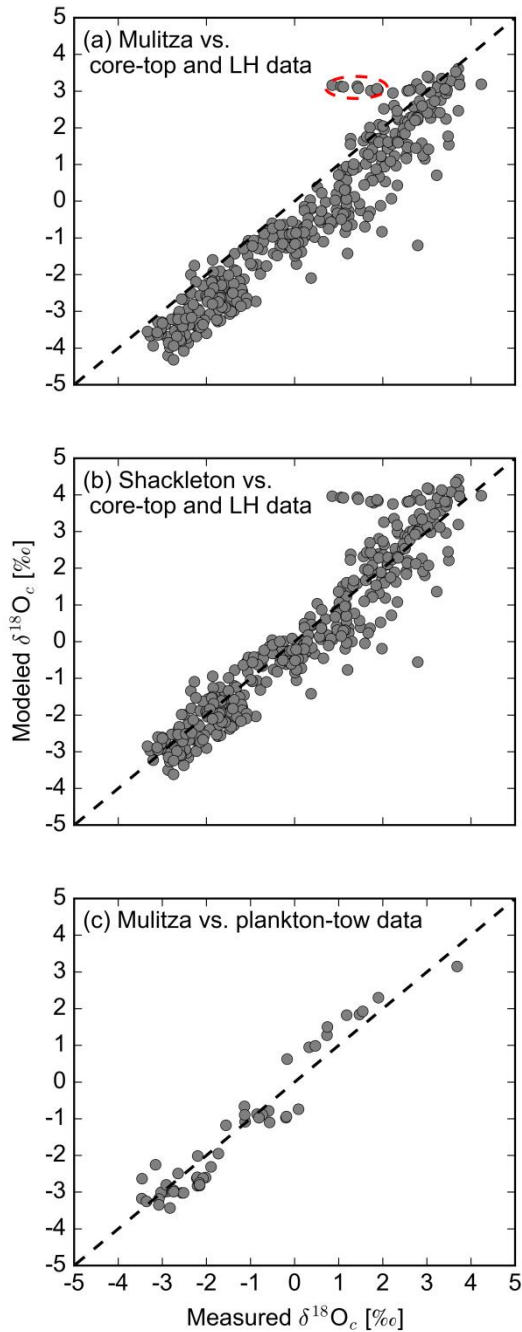
Figure 8: Relationship between measured $\delta^{18}O_c$ from various planktonic foraminiferas (core-top and Late Holocene (LH) - Waelbroeck et al., 2005) and modeled $\delta^{18}O_c$ from the MITgcm using the paleotemperature equation from Mulitza et al., 2004 (a) and Shackleton, 1974 (b). The red circle in (a) marks data points that do not fit to the observed systematic offset. The relationship between measured $\delta^{18}O_c$ from plankton tows (Duplessy et al., 1981, Kahn and Williams (1981), Ganssen 1983, Bauch et al., 1997 and Mulitza et al., 2003) and modeled $\delta^{18}O_c$ from the MITgcm using the paleotemperature equation from Mulitza et al., 2004 is displayed in (c). Dashed lines represent the 1:1 line.
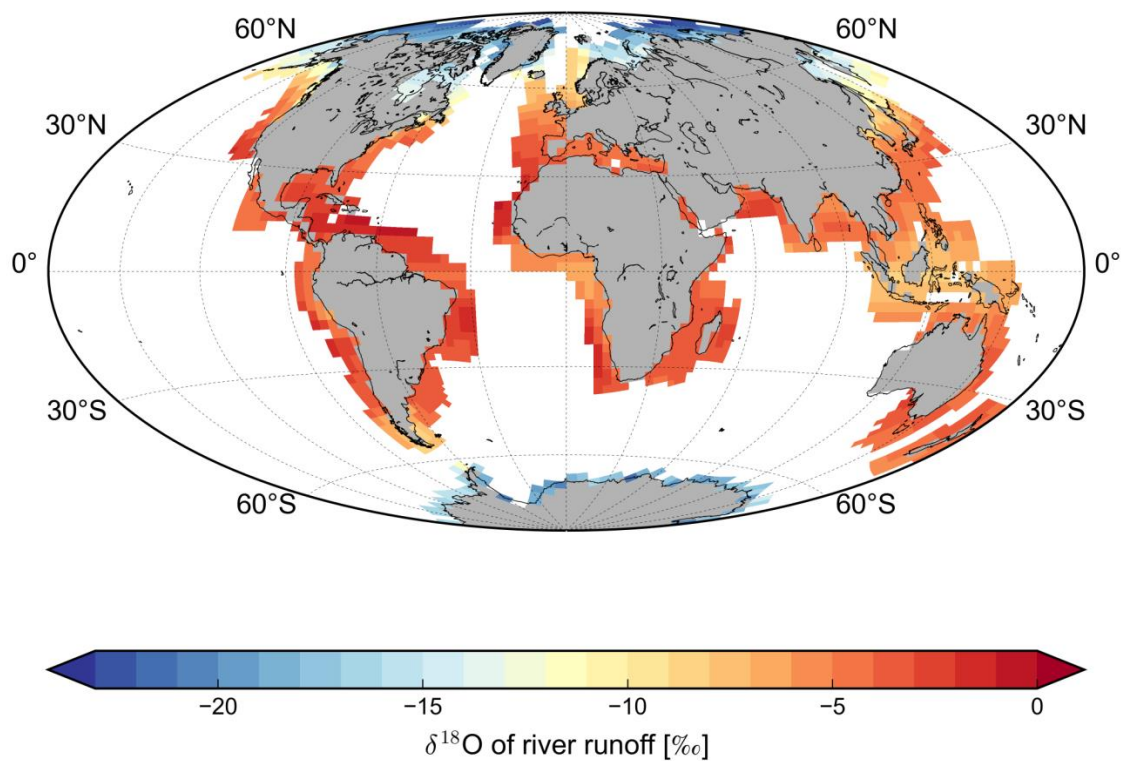
Figure 9: Simulated annual mean δ¹⁸O of river runoff.
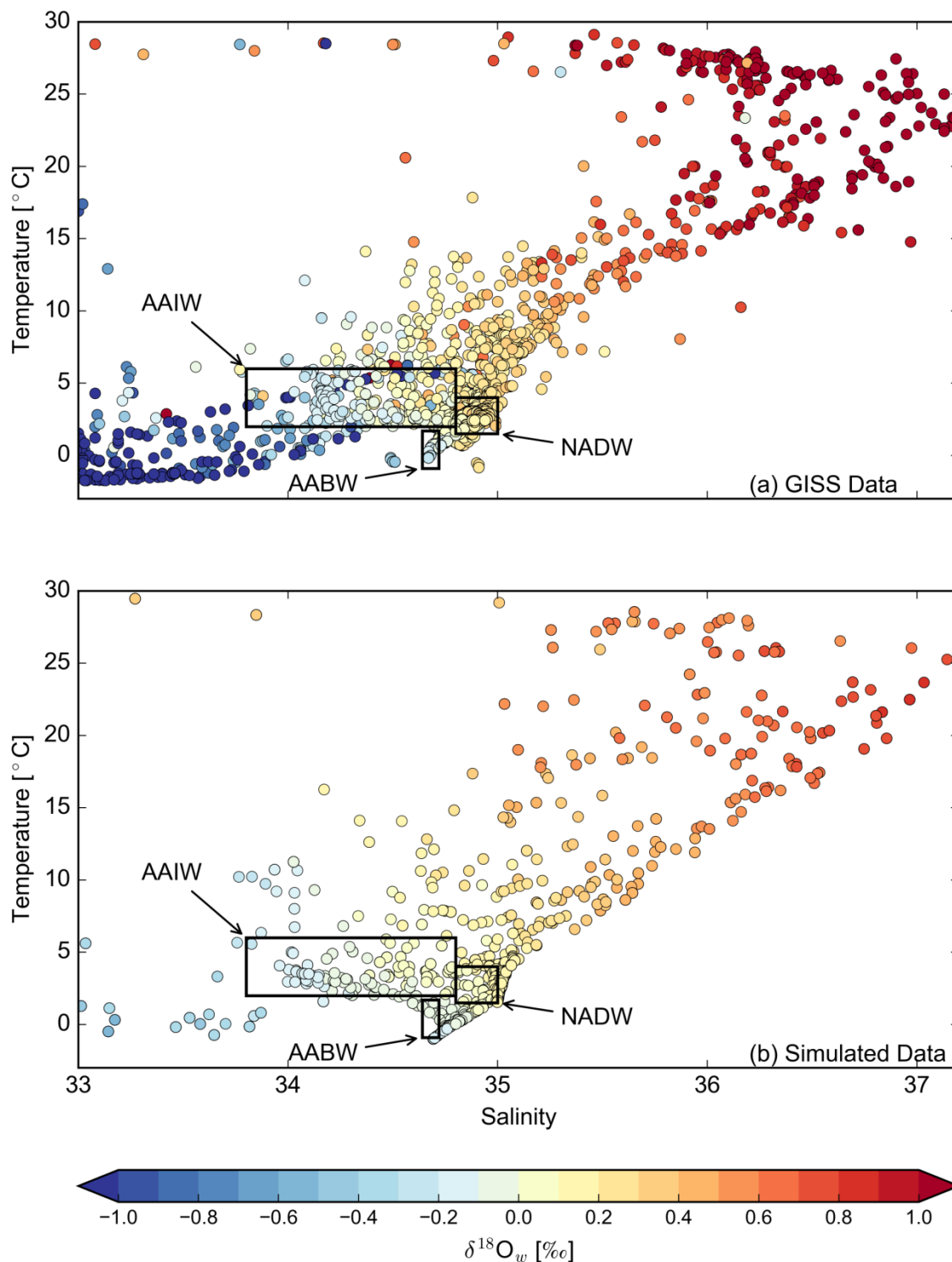
Figure 10: Combined T-S-δ¹⁸Oₓ diagrams for the (a) GISS data and (b) simulated data in the Atlantic Ocean. The temperature and salinity ranges for the different water masses in the Atlantic Ocean are defined according to Emery and Meincke (1986).
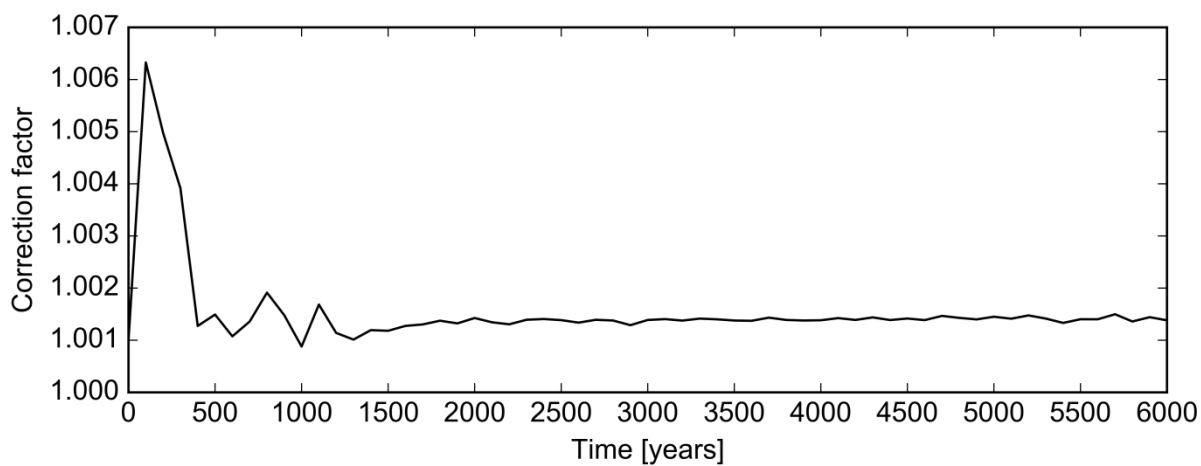
Figure A1: Time series of the precipitation correction factor throughout the model integration.